

Banner appropriate to article type will appear here in typeset article

Linear stability theory and molecular simulations of nanofilm dewetting with disjoining pressure, strong liquid-solid slip, and thermal fluctuations

Yixin Zhang¹†

¹Physics of Fluids Group, Max Planck Center Twente for Complex Fluid Dynamics and J. M. Burgers Centre for Fluid Dynamics, University of Twente, P.O. Box 217, 7500 AE Enschede, The Netherlands

(Received xx; revised xx; accepted xx)

The dewetting of thin nanofilms is significantly impacted by thermal fluctuations, liquid-solid slip, and disjoining pressure, which can be described by lubrication equations augmented by appropriately scaled noise terms, known as stochastic lubrication equations. Here molecular dynamics simulations along with a newly proposed slip-generating method are adopted to study the instability of nanofilms with arbitrary slip. These simulations show that strong-slip dewetting is distinct from weak-slip dewetting by faster growth of perturbations and fewer droplets after dewetting, which can not be predicted by the existing stochastic lubrication equation. A new stochastic lubrication equation considering the strong slip boundary condition is thus derived using a long-wave approximation to the equations of fluctuating hydrodynamics. The linear stability analysis of this equation, i.e., surface spectrum, agrees well with molecular simulations. Interestingly, strong slip can break down the usual Stokes limits adopted in weak-slip dewetting and bring the inertia into effect. The evolution of the standard deviation of the film height $W^2(t) = \overline{h^2} - \bar{h}^2$ at the initial stage of the strong-slip dewetting is found to be $W \sim t^{1/4}$ in contrast to $W \sim t^{1/8}$ for the weak-slip dewetting.

1. Introduction

Nanometric thin liquid films deposited on substrates exist in a host of applications such as in lubricants (Jhon *et al.* 1999), coatings (Weinstein & Ruschak 2004), and microfluidics (Stone *et al.* 2004). The reliability of those applications depends heavily on our understanding of their stability mechanism, which is usually investigated in the context of thin-film flows (Oron *et al.* 1997; Craster & Matar 2009). Thin-film flows are characterized by the disparity of length scale in different dimensions, i.e., the ratio of film height h to characteristic film length λ is very small: $\chi = h/\lambda \ll 1$. This allows the adoption of a long-wave theory to derive lubrication equations from the full governing equations and boundary conditions, reducing the dimensionality and complexity of the problems (Oron *et al.* 1997; Craster & Matar 2009).

Polymeric or metallic films on substrates with thicknesses below one hundred nanometers have been observed to undergo spontaneous rupture and dewetting (Xie *et al.* 1998; Seemann *et al.* 2001; Becker *et al.* 2003; González *et al.* 2016). The dewetting mechanism in these films may be complicated due to the contamination of defects in the liquid. However, the primary

† Email address for correspondence: Y.Zhang-11@utwente

dewetting mechanism for homogeneous liquid films is usually called spinodal dewetting. In this process, disjoining pressure, as a result of intermolecular forces between liquid and solid, leads to the instability of films. Basically, from the classical perspective, thermally excited capillary waves can be amplified by the disjoining pressure, but in competition with the restoring force of surface tension, such that disturbances above a critical wavelength can grow and lead to film rupture (Vrij & Overbeek 1968).

For interfacial flows at the nanoscale, thermal fluctuations can play an important role in the instability process (Moseler & Landman 2000; Grün *et al.* 2006; Zhang *et al.* 2019). Thermal fluctuations can spontaneously generate thermal capillary waves (TCW) and roughness on the free surface of a liquid film at rest. The magnitude of thermal roughness is usually proportional to thermal length $\sqrt{k_B T / \gamma}$ (k_B , T , and γ are the Boltzmann constant, temperature, and surface tension respectively) (Buff *et al.* 1965; MacDowell 2017). Though the roughness is small and usually on the scale of nanometres, it becomes comparable to the size of films when the film thickness goes down to several nanometers. Note that micrometer roughness can also be obtained and thus observed optically in real space using ultra-low surface tension mixtures ($\gamma \sim 10^{-6}$ N/m) (Aarts *et al.* 2004). In the equilibrium state, the amplitude of TCW, known as the static spectrum, can be described by the renowned capillary wave theory (Buff *et al.* 1965; MacDowell 2017; Höfling & Dietrich 2015, 2020, 2024). Recently, an extension of the capillary wave theory has been proposed utilizing a Langevin equation to describe the transient dynamics of non-equilibrium TCW and their approach to thermal equilibrium (Zhang *et al.* 2021). This advancement has led to the identification of a universality class governing the roughening behavior of film surfaces (Zhang *et al.* 2021).

The increasing importance of thermal fluctuations as the film height decreases may make the deterministic description of hydrodynamics at the nanoscale break down. For example, the breakup of liquid nanojets in molecular dynamics (MD) simulations (Moseler & Landman 2000; Zhao *et al.* 2019) and experiments (Hennequin *et al.* 2006) shows a double-cone rupture profile, in contrast to the long-thread profile predicted by the deterministic lubrication equation (Eggers & Dupont 1994). Moseler & Landman (2000) pioneered in showing that the deficiency of this deterministic lubrication equation for describing nanojet dynamics can be remedied by adding a noise term of appropriate strength to the equation, which leads to a stochastic lubrication equation for nanojets. Eggers (2002) later shows that the evolution of the minimum neck radius is accelerated by thermal fluctuations, leading to $h_{min} \propto (t_0 - t)^{0.418}$ (t_0 is the rupture time) in contrast with $h_{min} \propto (t_0 - t)$ for the deterministic pinching. This noise-dominated breakup for nanojets has been observed in experiments using ultra-low surface tension mixtures (Hennequin *et al.* 2006).

For nanofilm rupture, Grün *et al.* (2006) and Davidovitch *et al.* (2005) independently derived the same stochastic lubrication equation for liquid films on *no-slip* substrates. The numerical solution to this equation (Grün *et al.* 2006) can resolve the discrepancy in dewetting time between experimental results (Becker *et al.* 2003) and the solution to the deterministic counterpart. Subsequently, the rupture of thin films with the effects of thermal fluctuations has been widely investigated by numerical solutions to the stochastic film equation (Grün *et al.* 2006; Nestic *et al.* 2015; Diez *et al.* 2016; Durán-Olivencia *et al.* 2019; Shah *et al.* 2019). These studies have consistently demonstrated that thermal fluctuations indeed accelerate the rupture process. The application of this stochastic film equation is not restricted to nanofilm dewetting. It has been extended to study, for example, nanodroplet spreading under an elastic sheet (Carlson 2018), curvature-induced film drainage (Shah *et al.* 2019), and mediated diffusion of particles confined in channels with a fluctuating wall (Marbach *et al.* 2018).

In addition to numerical solutions, linear stability analyses of the stochastic film equation

have also been studied a lot, which allows us to obtain the evolution of the capillary spectra of surface waves (Mecke & Rauscher 2005; Fetzer *et al.* 2007; Zhao *et al.* 2019; Zhang *et al.* 2019). The analytical spectra show thermal fluctuations can massively amplify the growth of waves, shift the critical wavenumber to a larger value, and cause the dominant wavelength to evolve in time (in contrast to a constant value predicted by the deterministic lubrication equation). These interesting findings have been validated both in MD simulations (Zhang *et al.* 2019) and experiments (Fetzer *et al.* 2007).

The original stochastic film equation mentioned above adopts the classical *no-slip* boundary condition. As the flow scale reaches nanometers, surface effects like liquid-solid slip can have significant effects on flow behaviours (see the reviews by Lauga *et al.* (2005); Bocquet & Charlaix (2010)). Obviously, nanofilm flows can be significantly impacted by slip as well, since the ratio of slip length b to the film thickness h can get close to unity or even much larger than unity (Bäumchen & Jacobs 2009). In fact, in the deterministic setting, the introduction of slip to the deterministic film equation has been extensively studied for various phenomena, such as in coating a plate (Liao *et al.* 2013), droplet spreading (Savva *et al.* 2010), film rupture (Martínez-Calvo *et al.* 2020), falling films down a slippery plate (Ding & Wong 2015). However, only recently, the no-slip stochastic film equation is generalized to consider slip (Zhang *et al.* 2020), which is non-trivial and requires the usage of the Green-Kubo-type expression (Bocquet & Barrat 1994) that relates slip length to the random stress tensor at the wall. The derived slip equation is validated by the well-controlled molecular simulations (Zhang *et al.* 2020).

However, the derived slip equation (Zhang *et al.* 2020) is limited to the case of *weak slip* $b/h \approx 1$. In many cases, the slip length can be as large as micrometers so that $b/h \gg 1$, such as flow over graphene sheets (Falk *et al.* 2010), flow over engineered hydrophobic materials (Rothstein 2010), flow over substrates in presence of gas cavities and surface nanobubbles (Lohse & Zhang 2015). For polymer liquids, increasing molecular weights can also increase the slip length up to micrometers (Bäumchen *et al.* 2009). In fact, the dewetting of polymeric films on dodecyltrichlorosilane substrate (DTS), where slip length can be up to one micrometer, has been examined extensively in the deterministic framework (Fetzer *et al.* 2005; Münch *et al.* 2005; Kargupta *et al.* 2004; Bäumchen *et al.* 2014). Notably, different levels of slip give rise to different deterministic lubrication models (Münch *et al.* 2005). However, as we mentioned earlier, the effects of thermal fluctuations on nanofilms are significant, so a generalization of our current understanding of the instability of strong-slip films to consider thermal fluctuations is essential.

So far, experimental studies on the effects of thermal fluctuations on thin film flows are limited due to the technical difficulties associated with the spatiotemporal scale. Though the experiments of the dewetting of polymer nanofilms on no-slip SiO₂-coated silicon wafers have demonstrated the great effects of thermal fluctuations (Fetzer *et al.* 2007) on the growth of surface perturbations, dewetting of polymer films with strong slip and thermal fluctuations have not been considered in experiments. As such, molecular dynamics (MD) simulations are a natural and convenient tool to investigate the thin-film problem at the nanoscale as thermal fluctuations are inherent in MD simulations.

In this work, molecular dynamics simulations are employed to simulate the rupture of nanofilms on substrates with a strong slip, in comparison with the small-slip rupture. A new simulation strategy is proposed to generate strong slip in molecular simulations since the classic molecular simulations are limited to weak slip. We obtain the evolution of film surface spectra, rupture time, and number of droplets after film rupture from molecular simulations. A new stochastic lubrication equation considering the strong slip is derived from fluctuating hydrodynamics. A linear stability analysis of this stochastic lubrication equation leads to the

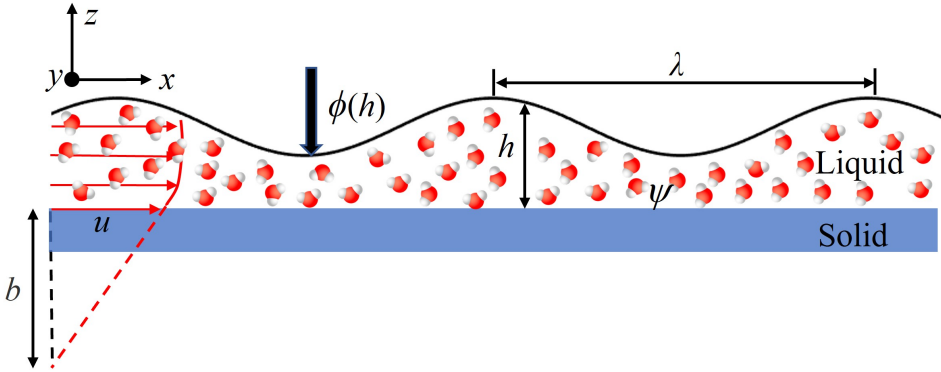


Figure 1: Sketch of a (quasi-two dimensional) molecularly thin liquid film on a slippery substrate. Here $h(x, t)$ is the film thickness, λ is the characteristic length, u is the horizontal velocity, ϕ is the disjoining pressure, and b is the slip length. The film has a small depth L_y into the page.

analytical spectra which are validated against the MD results to establish the applicability of the new theory to predict future experiments.

This paper is organized as follows. In § 2, the stochastic lubrication equation for the strong-slip dewetting is derived from the equations of fluctuating hydrodynamics using a long-wave approximation. In § 3, a linear stability analysis of the newly derived stochastic equation is performed to obtain the surface spectrum. In § 4, molecular simulations of the rupture of nanofilms with the method to generate strong slip are presented. § 5 compares the new model with molecular simulation results, and discusses new findings. In § 6, we summarise the main contributions of this work and outline future directions of research.

2. Stochastic lubrication equation for films with strong slip

2.1. Governing equations and boundary conditions

As shown in figure 1, a molecularly thin liquid film is deposited on a solid surface and destabilized by both disjoining pressure ϕ and thermal fluctuations ψ . The film is quasi-two dimensional (2D) confined by its size (L_x, L_y, h) where $L_x \gg L_y$ and $L_x \gg h$. Without slip, the stochastic thin film equation is derived in detail by Grün *et al.* (2006) using a long-wave approximation ($\chi = h_0/\lambda \ll 1$) to fluctuating hydrodynamics (FH) (Landau & Lifshitz 1959). The no-slip stochastic equation has been extended to consider weak slip $b \sim O(h)$ (Zhang *et al.* 2020). Here we present the derivation of a new equation considering $b \gg h$.

The governing equations for this problem are given by equations of FH, where thermal fluctuations are modelled by an additional random stress tensor. The (incompressible) continuum equation and momentum equations are

$$\partial_x u + \partial_z w = 0, \quad (2.1)$$

$$\rho (\partial_t u + u \partial_x u + w \partial_z u) = -\partial_x p + \mu (\partial_{xx} u + \partial_{zz} u) + \partial_x \psi_{xx} + \partial_z \psi_{zx}, \quad (2.2)$$

$$\rho (\partial_t w + u \partial_x w + w \partial_z w) = -\partial_z p + \mu (\partial_{xx} w + \partial_{zz} w) + \partial_x \psi_{xz} + \partial_z \psi_{zz}. \quad (2.3)$$

Here u and w are the x and z components of velocity, and ψ is a 2D random stress tensor

with zero mean and covariance given by

$$\langle \psi_{ij}(\mathbf{x}, t) \psi_{lm}(\mathbf{x}', t') \rangle = \frac{2\mu k_B \theta}{L_y} (\delta_{il} \delta_{jm} + \delta_{im} \delta_{jl}) \delta(x - x') \delta(z - z') \delta(t - t'). \quad (2.4)$$

Here θ is the temperature. The factor $1/L_y$ appears because the films are quasi-2D ($L_y \ll L_x$), allowing all variables of interest to be averaged over the y direction (Zhang *et al.* 2020).

For boundary conditions, at $z = h$, we have the dynamic condition and kinematic condition:

$$(\boldsymbol{\sigma} + \boldsymbol{\psi}) \cdot \mathbf{n} = -[\gamma \nabla \cdot \mathbf{n} + \phi(h)] \mathbf{n}, \quad \partial_t h + u \partial_x h = w \quad \text{at} \quad z = h. \quad (2.5a,b)$$

Here $\boldsymbol{\sigma} = -p \delta_{ij} + \mu (\partial_{x_j} u_i + \partial_{x_i} u_j)$ is the hydrodynamic stress tensor (here $i = (x, z)$ and $j = (x, z)$), γ is the surface tension, $\phi(h)$ is the disjoining pressure, and \mathbf{n} is the outer normal vector at the surface $\mathbf{n} = (-\partial_x h, 1) / \sqrt{1 + (\partial_x h)^2}$.

At $z = 0$, the impermeable condition and Navier's slip boundary condition are separately given by

$$w = 0, \quad u = b \frac{\partial u}{\partial z}, \quad \text{at} \quad z = 0. \quad (2.6a,b)$$

where b is the slip length. The covariance of the random shear stress at the wall is given by (Bocquet & Barrat 1994; Zhang *et al.* 2020):

$$\langle \psi_{zx}|_{z=0}(x, t) \psi'_{zx}|_{z=0}(x', t') \rangle = \frac{2\mu k_B \theta}{b L_y} \delta(x - x') \delta(t - t'). \quad (2.7)$$

Navier's slip condition is chosen because it has been extensively validated by both experiments and MD simulations (see the reviews by Lauga *et al.* (2005); Bocquet & Charlaix (2010)). However, there are many other forms of slip boundary conditions, as discussed by Sibley *et al.* (2015).

2.2. A long wave approximation

To derive a lubrication equation, (2.1)-(2.6a,b) have to be scaled based on the dominant mechanism of momentum balance, which varies with the level of slip length (Münch *et al.* 2005). Classically, for the weak-slip case, the momentum balance happens in the horizontal direction $\partial_x p \sim \mu \partial_{zz} u$, which means $ph_0/(\mu u_0) \sim 1/\chi$, where u_0 is the characteristic velocity. At the free surface, surface tension has to be balanced with pressure $p = -\gamma \partial_{xx} h$, which means $\gamma/(\mu u_0) \sim 1/\chi^3$. At the solid surface, the order of slip length is $b \sim h_0$. Therefore, the pressure term, surface tension term, and slip length will be scaled to $P = \chi ph_0/(\mu u_0)$, $\Gamma = \chi^3 \gamma/(\mu u_0)$, and $B = b/h_0$.

However, for the strong-slip (including free slip) flow, the velocity profile essentially becomes uniform (plug flow) instead of being parabolic so that the momentum balance happens in the vertical direction $\partial_z p \sim \mu \partial_{zz} w$ (Münch *et al.* 2005), which leads to the scaling $ph_0/(\mu u_0) \sim \chi$ and $\gamma/(\mu u_0) \sim 1/\chi$. These scalings need the slip length to be strong and $b \sim h_0 \chi^{-2}$ (Münch *et al.* 2005).

As for the scaling of the random stress tensor, it may be scaled the same as the scale of their deterministic counterparts (Grün *et al.* 2006). For example, $\psi_{xx} \sim \mu \partial_x u \sim \mu u_0/\lambda$ and $\psi_{zz} \sim \mu \partial_z w \sim \mu u_0/\lambda$. Note in this way, two scaling exists for ψ_{zx} : $\psi_{zx} \sim \mu \partial_x w \sim \mu \chi u_0/\lambda$ and $\psi_{zx} \sim \mu \partial_z u \sim \mu u_0/(\chi \lambda)$. The former one is used to keep ψ_{zx} at a lower order. In

summary, the following scalings are used:

$$\begin{aligned} X &= \frac{x}{\lambda}, Z = \frac{z}{h_0}, H = \frac{h}{h_0}, B = \frac{b}{h_0 \chi^{-2}}, U = \frac{u}{u_0}, W = \frac{w}{\chi u_0}, T = \frac{u_0 t}{\lambda}, \Gamma = \frac{\chi \gamma}{\mu u_0}, \\ (P, \Phi) &= \frac{h_0}{\chi u_0 \mu} (p, \phi), (\Psi_{xx}, \Psi_{zz}) = \frac{\lambda}{u_0 \mu} (\psi_{xx}, \psi_{zz}), (\Psi_{xz}, \Psi_{zx}) = \frac{\lambda}{\chi u_0 \mu} (\psi_{xz}, \psi_{zx}). \end{aligned} \quad (2.8)$$

Adopting these scalings (2.8), the rescaled and dimensionless continuum and momentum equations are

$$\partial_X U + \partial_Z W = 0, \quad (2.9)$$

$$\chi \operatorname{Re} (\partial_T U + U \partial_X U + W \partial_Z U) = -\chi^2 \partial_X P + \chi^2 \partial_{XX} U + \partial_{ZZ} U + \chi^2 \partial_X \Psi_{xx} + \chi^2 \partial_Z \Psi_{zx}, \quad (2.10)$$

$$\chi \operatorname{Re} (\partial_T W + U \partial_X W + W \partial_Z W) = -\partial_Z P + \chi^2 \partial_{XX} W + \partial_{ZZ} W + \chi^2 \partial_X \Psi_{xz} + \partial_Z \Psi_{zz}. \quad (2.11)$$

Here the Reynolds number is $\operatorname{Re} = \rho u_0 h_0 / \mu$. As the characteristic velocity is $u_0 \sim \chi \gamma / \mu$, the Re can be also written as $\operatorname{Re} = \chi \rho \gamma h_0 / \mu^2 = \chi \operatorname{La}$, where $\operatorname{La} = \rho \gamma h_0 / \mu^2$ is the Laplace number. The La is assumed to be of order one.

In terms of the rescaled boundary conditions,

$$\begin{aligned} -P + \frac{1}{1 + \chi^2 (\partial_X H)^2} \left\{ 2 [1 - \chi^2 (\partial_X H)^2] \partial_Z W - 2 \partial_X H (\partial_Z U + \chi^2 \partial_X W) + \chi^2 (\partial_X H)^2 \Psi_{xx} - \right. \\ \left. \chi^2 \partial_X H (\Psi_{xz} + \Psi_{zx}) + \Psi_{zz} \right\} = \Gamma \frac{\partial_{XX} H}{[1 + \chi^2 (\partial_X H)^2]^{3/2}} + \Phi \quad \text{at } z = H, \end{aligned} \quad (2.12a)$$

$$\begin{aligned} 2\chi^2 \partial_X H \left[(\partial_Z W - \partial_X U) + \frac{1}{2} (\Psi_{zz} - \Psi_{xx}) \right] + [1 - \chi^2 (\partial_X H)^2] (\partial_Z U + \chi^2 \partial_X W + \chi^2 \Psi_{zx}) = 0 \\ \text{at } z = H, \end{aligned} \quad (2.12b)$$

$$\partial_T H + U \partial_X H = W \quad \text{at } z = H. \quad (2.12c)$$

$$W = 0 \quad \text{at } z = 0, \quad (2.12d)$$

$$U = \frac{B}{\chi^{-2}} \partial_Z U \quad \text{at } z = 0. \quad (2.12e)$$

The rescaled equations can be approximately solved by the perturbation expansion of U, W, P, Ψ, H :

$$(U, W, P, \Psi, H) = (U_0, W_0, P_0, \Psi_0, H_0) + \chi^2 (U_1, W_1, P_1, \Psi_1, H_1) + \dots \quad (2.13)$$

Then, at leading orders of governing equations, one can get

$$\partial_{ZZ} U_0 = 0, \quad (2.14)$$

$$\partial_{ZZ} W_0 - \partial_Z P_0 + \partial_Z \Psi_{zz0} = 0, \quad (2.15)$$

$$\partial_X U_0 + \partial_Z W_0 = 0, \quad (2.16)$$

For boundary conditions, their leading-order forms are

$$-P_0 + 2 (\partial_Z W_0 - \partial_X H_0 \partial_Z U_0) + \Psi_{zz0} = \Gamma \partial_{XX} H_0 + \Phi \quad \text{at } z = H, \quad (2.17a)$$

$$\partial_Z U_0 = 0 \quad \text{at } z = H, \quad (2.17b)$$

$$W_0 = \partial_T H_0 + U_0 \partial_X H_0 \quad \text{at } z = H, \quad (2.17c)$$

$$W_0 = 0 \quad \text{at} \quad z = 0, \quad (2.17d)$$

$$\partial_Z U_0 = 0 \quad \text{at} \quad z = 0. \quad (2.17e)$$

Using leading order equations, we find

$$U_0 \equiv U_0(X, T), \quad (2.18)$$

$$W_0 = -\partial_X U_0 Z, \quad (2.19)$$

$$P_0 = -2\partial_X U_0 - \Gamma \partial_{XX} H_0 - \Phi + \Psi_{zz0}, \quad (2.20)$$

which leads to the first equation of the desired stochastic lubrication equation:

$$\partial_T H_0 + \partial_X (H_0 U_0) = 0. \quad (2.21)$$

In the next order, the governing equation that will be used is,

$$\text{La} (\partial_T U_0 + U_0 \partial_X U_0) = \partial_{XX} U_0 - \partial_X P_0 + \partial_{ZZ} U_1 + \partial_X \Psi_{xx0} + \partial_Z \Psi_{zx0} \quad (2.22)$$

and the boundary condition that will be needed is

$$-4\partial_X H_0 \partial_X U_0 + \partial_X H_0 (\Psi_{zz0} - \Psi_{xx0}) + \partial_Z U_1 - H_0 \partial_{XX} U_0 + \Psi_{zx0} = 0, \quad \text{at} \quad z = H, \quad (2.23)$$

$$U_0 = B \partial_Z U_1, \quad \text{at} \quad z = 0. \quad (2.24)$$

Integrating (2.22) from 0 to H_0 and using boundary conditions (2.23) and (2.24) leads to

$$\begin{aligned} H_0 [\text{La} (\partial_T U_0 + U_0 \partial_X U_0)] &= H_0 [3\partial_{XX} U_0 + \partial_X (\Gamma \partial_{XX} H_0 + \Phi)] \\ &+ (\partial_Z U_1 + \Psi_{zx0})|_{Z=H_0} - (\partial_Z U_1 + \Psi_{zx0})|_{Z=0} + \int_0^{H_0} \partial_X (\Psi_{xx0} - \Psi_{zz0}) dZ \\ &= H_0 \partial_X (\Gamma \partial_{XX} H_0 + \Phi) + 4\partial_X (H_0 \partial_X U_0) - \frac{U_0}{B} + \partial_X \int_0^{H_0} (\Psi_{xx0} - \Psi_{zz0}) dZ - \Psi_{zx0}|_{Z=0}. \end{aligned} \quad (2.25)$$

The Leibniz integral rule is used here. The covariance of $\Psi_{zx0}|_{Z=0}$ is given by the Green-Kubo expression for slip length $\langle \Psi_{zx}|_{Z=0}(X, T) \Psi'_{zx}|_{Z=0}(X', T') \rangle = \frac{2k_B \theta}{\chi^2 \mu u_0 b L_y} \delta(X - X') \delta(T - T')$ (Zhang *et al.* 2020). In terms of the integral of the white noise in (2.25), as Ψ_{xx0} is uncorrelated with Ψ_{zz0} , they can be combined as $\sqrt{2} \Psi_{xx0}$. Now using the theorem provided in the appendix of Zhang *et al.* (2020), the integral of the white noise is

$$\begin{aligned} \partial_X \int_0^{H_0} (\Psi_{xx0} - \Psi_{zz0}) dz &= \sqrt{2} \partial_X \int_0^{H_0} \Psi_{xx0} dz \\ &= \sqrt{2} \partial_X \left(\sqrt{H_0} \mathfrak{X} \right), \end{aligned} \quad (2.26)$$

where $\langle \mathfrak{X}(X, T) \mathfrak{X}(X', T') \rangle = \frac{4k_B \theta}{\mu u_0 h_0 L_y} \delta(X - X') \delta(T - T')$.

Putting (2.21) and (2.25) together and returning to their dimensional forms, we arrive at the stochastic lubrication equation for films with strong slip (referred to as S-S model hereafter)

$$\partial_t h + \partial_x (hu) = 0, \quad (2.27a)$$

$$\rho (\partial_t u + u \partial_x u) = \partial_x (-\gamma \partial_{xx} h + \phi) + \frac{4\mu}{h} \partial_x (h \partial_x u) - \frac{\mu}{h} \frac{u}{b} + \frac{1}{h} \left[2\partial_x \left(\sqrt{h} \xi_1 \right) - \frac{\sqrt{b}}{b} \xi_2 \right] \quad (2.27b)$$

where the covariance of the noise term is $\langle \xi_i(x, t) \xi_j(x', t') \rangle = \frac{2\mu k_B \theta}{L_y} \delta_{ij} \delta(x - x') \delta(t - t')$.

The above derived stochastic lubrication equation validates for the strong slip length on the order of $b \sim h_0 \chi^{-2}$. In terms of the weak slip $b \sim h_0$, a similar long-wave approximation to FH equations (see Zhang *et al.* (2020) for details) can result in the weak-slip stochastic lubrication equation (referred to as W-S model hereafter)

$$\partial_t h = \frac{1}{\mu} \partial_x \left[\left(\frac{1}{3} h^3 + b h^2 \right) \partial_x (-\gamma \partial_{xx} h + \phi) + \sqrt{\frac{1}{3} h^3 + b h^2} \xi_3 \right], \quad (2.28)$$

where the noise ξ_3 has zero mean and covariance $\langle \xi_3(x, t) \xi_3(x', t') \rangle = \frac{2\mu k_B \theta}{L_y} \delta(x - x') \delta(t - t')$. As the W-S model works for the no-slip case ($b = 0$), the S-S model validates for the free-slip case ($b = \infty$) where the terms containing b in (2.27) vanish. Interestingly, this free-slip model can be applied to study free films such as foam films (Erneux & Davis 1993; Vaynblat *et al.* 2001). Note that the free-slip model has not been reported before.

3. Surface spectrum for films with strong slip

With the newly developed S-S model (2.27), the spectrum of surface waves in linear stages is derived here. We firstly rewrite the noise ξ in terms of the white noise N with unit variance $\langle N_i N_j' \rangle = \delta_{ij} \delta(x - x') \delta(t - t')$, and linearise (2.27) with $h = h_0 + \tilde{h}$, $u = 0 + \tilde{u}$, and $N = 0 + \tilde{N}$:

$$\frac{\partial^2 \tilde{h}}{\partial t^2} = \frac{\mu}{\rho} \frac{\partial}{\partial t} \left[4 \frac{\partial^2 \tilde{h}}{\partial x^2} - \frac{\tilde{h}}{h_0 b} \right] - \frac{h_0}{\rho} \left[\frac{\partial \phi}{\partial h} \frac{\partial^2 \tilde{h}}{\partial x^2} + \gamma \frac{\partial^4 \tilde{h}}{\partial x^4} \right] - f_1 \frac{\partial^2 \tilde{N}_1}{\partial x^2} + f_2 \frac{\partial \tilde{N}_2}{\partial x}, \quad (3.1)$$

where the factor $f_1 = \sqrt{8\mu k_B \theta h_0 L_y} / (\rho L_y)$ and $f_2 = \sqrt{2\mu k_B \theta b L_y} / (\rho b L_y)$. Note that the second derivative of \tilde{h} with respect to t comes from putting the linearized (2.27)(a) into the linearized (2.27)(b) to eliminate the variable \tilde{u} . Then a Fourier transform of (3.1) is performed using $\hat{h}(q, t) = \int_{-\infty}^{\infty} \tilde{h}(x, t) e^{-iqx} dx$ and $\hat{N}(q, t) = \int_{-\infty}^{\infty} \tilde{N}(x, t) e^{-iqx} dx$ to get

$$\frac{\partial^2 \hat{h}}{\partial t^2} = -C \frac{\partial \hat{h}}{\partial t} - D \hat{h} + f_1 q^2 \hat{N}_1 + f_2 q i \hat{N}_2. \quad (3.2)$$

Here $C = \frac{\mu}{\rho} \left(4q^2 + \frac{1}{h_0 b} \right)$, $D = \frac{h_0}{\rho} \left[\frac{\partial \phi}{\partial h} q^2 + \gamma q^4 \right]$. The solution of (3.2) can be represented as the linear superposition of two contributions (Zhao *et al.* 2019; Zhang *et al.* 2019)

$$\hat{h} = \hat{h}_{\text{det}} + \hat{h}_{\text{sto}}, \quad (3.3)$$

where \hat{h}_{det} is the solution to the deterministic part of (3.2) and \hat{h}_{sto} is the contribution purely caused by thermal fluctuations. To find \hat{h}_{det} , the deterministic equation

$$\frac{\partial^2 \hat{h}}{\partial t^2} + C \frac{\partial \hat{h}}{\partial t} + D \hat{h} = 0, \quad (3.4)$$

is solved by Laplace transform. Using $g(q, s) = \int_0^{\infty} \hat{h}(q, t) e^{-its} dt$ and assuming $\frac{\partial \hat{h}}{\partial t} \Big|_{t=0} = 0$, one can get

$$g = \frac{s + C}{s^2 + Cs + D} \hat{h}(q, 0), \quad (3.5)$$

whose inverse Laplace transform is

$$\hat{h}_{\text{det}}(q, t) = \hat{h}(q, 0) \left[\frac{e^{\omega_1 t} + e^{\omega_2 t}}{2} + \frac{C}{2\sqrt{C^2 - 4D}} (e^{\omega_1 t} - e^{\omega_2 t}) \right] \quad (3.6)$$

Here $\omega_{i=1,2} = \frac{-C \pm \sqrt{C^2 - 4D}}{2}$ is the solution to $s^2 + Cs + D = 0$. Notably, ω_1 is the dispersion relation (growth rate) of the deterministic lubrication equation, namely, (2.27) without the noise terms.

To obtain \hat{h}_{sto} , one has to determine the impulse response of the linear system. Using the Laplace transform of $\frac{\partial^2 \hat{h}}{\partial t^2} + C \frac{\partial \hat{h}}{\partial t} + D \hat{h} = \delta$, and assuming $\hat{h}(q, 0) = 0$, it is found

$$g = \frac{1}{s^2 + Cs + D}. \quad (3.7)$$

The impulse response is thus the inverse Laplace transform of (3.7)

$$F(q, t) = \hat{h} = \frac{e^{\omega_1 t} - e^{\omega_2 t}}{\sqrt{C^2 - 4D}}. \quad (3.8)$$

Now with thermal fluctuations $f_1 q^2 \hat{N}_1$ and $f_2 q i \hat{N}_2$ as input, we find

$$\hat{h}_{\text{sto}} = f_1 q^2 \int_0^t \hat{N}_1(q, t - \tau) F(q, \tau) d\tau + f_2 q i \int_0^t \hat{N}_2(q, t - \tau) F(q, \tau) d\tau. \quad (3.9)$$

As \hat{h} is both a random and complex variable, the root mean square (RMS) of its norm is sought, namely, surface spectrum,

$$\left| \hat{h}(q, t) \right|_{\text{rms}} = \sqrt{\overline{|\hat{h}_{\text{det}} + \hat{h}_{\text{sto}}|^2}} = \sqrt{\overline{|\hat{h}_{\text{det}}|^2} + \overline{|\hat{h}_{\text{sto}}|^2}}, \quad (3.10)$$

where from (3.6)

$$\left| \hat{h}_{\text{det}} \right|^2 = \overline{|\hat{h}(q, 0)|^2} \left[\frac{e^{\omega_1 t} + e^{\omega_2 t}}{2} + \frac{C}{2\sqrt{C^2 - 4D}} (e^{\omega_1 t} - e^{\omega_2 t}) \right]^2, \quad (3.11)$$

and from (3.9)

$$\begin{aligned} \overline{|\hat{h}_{\text{sto}}|^2} &= \left| f_1 q^2 \int_0^t \hat{N}_1(q, t - \tau) F(q, \tau) d\tau \right|^2 + \left| f_2 q i \int_0^t \hat{N}_2(q, t - \tau) F(q, \tau) d\tau \right|^2 \\ &= |f_1 q^2|^2 \int_0^t \left| \hat{N}_1(q, t - \tau) \right|^2 F(q, \tau)^2 d\tau + |f_2 q i|^2 \int_0^t \left| \hat{N}_2(q, t - \tau) \right|^2 F(q, \tau)^2 d\tau \\ &= \left(|f_1 q^2|^2 + |f_2 q i|^2 \right) L_x \int_0^t F(q, \tau)^2 d\tau \\ &= \frac{2\mu k_B T L_x q^2}{\rho^2 L_y (C^2 - 4D)} \left(4h_0 q^2 + \frac{1}{b} \right) \left[\frac{e^{2\omega_1 t} - 1}{2\omega_1} + \frac{e^{2\omega_2 t} - 1}{2\omega_2} + \frac{2(e^{-Ct} - 1)}{C} \right]. \end{aligned} \quad (3.12)$$

Here we have used $\overline{|\hat{N}(q, t)|^2} = L_x$, due to the finite length of the discrete Fourier transform used in MD simulations. Thus, we derive the spectrum of surface waves of a bounded film with strong slip as,

$$\begin{aligned} S(q, t) &= \left\{ \overline{|\hat{h}(q, 0)|^2} \left[\frac{e^{\omega_1 t} + e^{\omega_2 t}}{2} + \frac{C}{2\sqrt{C^2 - 4D}} (e^{\omega_1 t} - e^{\omega_2 t}) \right]^2 \right. \\ &\quad \left. + \frac{2\mu k_B T L_x q^2}{\rho^2 L_y (C^2 - 4D)} \left(4h_0 q^2 + \frac{1}{b} \right) \left[\frac{e^{2\omega_1 t} - 1}{2\omega_1} + \frac{e^{2\omega_2 t} - 1}{2\omega_2} + \frac{2(e^{-Ct} - 1)}{C} \right] \right\}^{1/2} \end{aligned} \quad (3.13)$$

(3.13) and (2.27) are main contributions of this work. For the W-S model, its analytical spectrum is (Zhang *et al.* 2020)

$$S(q, t) = \sqrt{\left| \widehat{h}(q, 0) \right|^2 e^{2\omega_3(q)t} + \frac{L_x}{L_y} \frac{k_B T}{\gamma q^2 + (d\phi/dh)|_{h_0}} [1 - e^{2\omega_3(q)t}]}, \quad (3.14)$$

where the dispersion relation is

$$\omega_3 = -\frac{h_0^3 + bh_0^2}{3\mu} \left(\gamma q^4 + \frac{d\phi}{dh} \Big|_{h_0} q^2 \right). \quad (3.15)$$

4. Molecular simulations and a new slip-generating method

Molecular dynamics (MD) simulations are performed to simulate the instability of nanofilms on the strong-slip solid and the weak-slip solid. The open-source MD code LAMMPS (Plimpton 1995) is adopted. As shown in figure 2(a), the liquid film is composed of liquid Argon (represented in orange) and it is simulated with the standard Lennard-Jones (LJ) 12-6 potential:

$$U(r_{ij}) = \begin{cases} 4\varepsilon \left[\left(\frac{\sigma}{r_{ij}} \right)^{12} - \left(\frac{\sigma}{r_{ij}} \right)^6 \right] & \text{if } r_{ij} \leq r_c, \\ 0 & \text{if } r_{ij} > r_c. \end{cases} \quad (4.1)$$

Here r_{ij} is the distance between two atoms and ij represents pairwise particles. The energy parameter ε is 1.67×10^{-21} J and the length parameter σ is 0.34 nm. $r_c = 5.5\sigma$ is the cut-off distance, beyond which the interaction vanishes.

The temperature of this system is kept at $T = 85$ K using the Nosé-Hoover thermostat. At this temperature, the mass density is $\rho = 1.4 \times 10^3$ kg/m³ and the number density is $n = 0.83/\sigma^3$. The density of the vapor phase is about $(1/400)\rho$ so that the effects of vapor on the film are neglected. The surface tension of liquid is $\gamma = 1.52 \times 10^{-2}$ N/m and the dynamic viscosity is $\mu = 2.87 \times 10^{-4}$ kg/(ms) (Zhang *et al.* 2020). The time step for all simulations is $0.004\sqrt{\varepsilon/(m\sigma^2)}$ where m is the atomic mass of argon.

The initial dimensions of the liquid film (see figure 2(a)) are chosen as $L_x = 313.90$ nm, $L_y = 3.14$ nm. The height of the film varies for three different cases ($h_0 = 1.2$ nm, 1.6 nm, and 3.14 nm). Therefore, the film is thin ($L_x \gg h_0$), and the film is quasi-2D ($L_x \gg L_y$) to save computational costs. To prepare the initial configuration of the liquid film, the liquid film slab with the desired size is cut from a periodic box of liquid atoms, which makes the film surface flat initially.

Conventionally, the solid wall, serving as the boundary condition for the film, is simulated using real solid atoms (real wall) (Willis & Freund 2009; Zhang *et al.* 2019, 2020, 2021). In our previous work (Zhang *et al.* 2019, 2020, 2021), for a real wall, the solid is Platinum with its isotropic $\langle 100 \rangle$ surface in contact with the liquid. The liquid-solid interactions are modelled by the same 12-6 LJ potential with $\sigma_{ls} = 0.8\sigma$ for the length parameter and $\varepsilon_{ls} = k\varepsilon$. Conventionally, one may vary the energy parameter ε_{ls} to obtain different levels of slip length. For example, $b = 0.68$ nm using $k = 0.65$ while $b = 8.8$ nm using $k = 0.2$ (Zhang *et al.* 2021). The disjoining pressure and contact angles of liquid argon on the solid are also changed in this way. However, the slip length obtained using the real solid is usually in the range of a few ten nanometers (Bocquet & Charlaix 2010) in MD simulations, which cannot match the micrometer slip length present in experiments. The origin of strong slip in experiments, as discussed earlier in the Introduction, is usually complicated and cannot be straightforwardly simulated in previous MD simulations using LJ potentials. The use of a

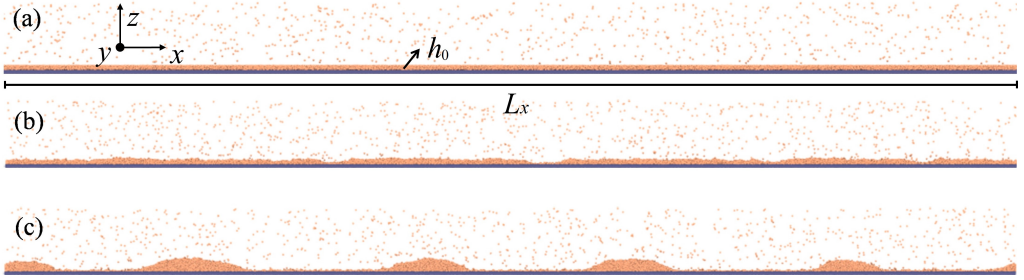


Figure 2: Rupture of thin liquid films with strong slip in molecular simulations. (a) initial setting of a liquid film with a flat free surface. The film has a small depth L_y into the page. (b) growth of perturbations and film rupture. (c) droplets formation after that the film ruptures. Note that the wall colored in blue only denotes the position of the solid boundary as the method of a virtual wall is used in simulations.

real solid wall with a cutoff-distance limited intermolecular interactions between liquid and solid also means that the disjoining pressure *due to the solid* vanishes when the film height is larger than the cutoff distance (Willis & Freund 2009; Zhang & Ding 2023), which is undesired.

Here we propose a new approach to allow us to generate any values of slip length simply in MD simulations and allow disjoining pressure to be effective at infinite distances physically. Instead of simulating a real wall, we apply a force to fluid atoms to mimic the fluid-substrate interactions and the force acts as the virtual wall, based on the work of (Steele 1973; Barrat & Bocquet 1999; Hadjiconstantinou 2021). The (total) force \vec{f} for a fluid atom interacting with a face-centered-cubic solid substrate by the LJ potential has been calculated analytically by Steele (1973) and it is adopted here with some modifications (see Appendix for detailed discussions):

$$\begin{aligned} \vec{f} &= f_x \vec{e}_x + f_z \vec{e}_z, \quad \text{with} \\ f_x &= \frac{(2\pi)^2 \varepsilon}{100 \ell_s^3} \left[\frac{\sigma^{12}}{30} \left(\frac{\pi}{\ell_s z} \right)^5 K_5 \left(\frac{2\pi}{\ell_s} z \right) - 2\sigma^6 \left(\frac{\pi}{\ell_s z} \right)^2 K_2 \left(\frac{2\pi}{\ell_s} z \right) \right] \sin \left(\frac{2\pi}{\ell_s} x \right), \\ f_z &= -\frac{dU_0(z)}{dz} \end{aligned} \quad (4.2)$$

Here \vec{e}_x and \vec{e}_z are unit vectors in the x and z direction. ℓ_s is the lattice spacing. The K_5 and K_2 are the modified Bessel function of the second kind. The applied force in the x direction f_x decays rapidly with z . f_x is closely related to slip length and its sinusoidal-form force represents the energy corrugation of the solid surface. A smaller lattice spacing ℓ_s results in a smooth surface energy distribution and then a larger slip length (Thompson & Robbins 1990; Barrat & Bocquet 1999; Hadjiconstantinou 2021). In our MD simulations, the function K_5 and K_2 are approximated by $(\frac{\pi}{2x})^{1/2} e^{-x}$ for simplicity. Here $U_0(z)$ is the total interaction energy exerted on a liquid molecule by the (continuous) substrate. As shown in Appendix, $U_0(z)$ is related to the function of disjoining pressure as $U_0(z) = -\phi(z)/n$. Note that disjoining pressure is a function of film height h . One has to replace h with z while the form of the function itself is the same.

Here ϕ takes the usual form (Israelachvili 2011):

$$\phi(h) = \frac{A}{6\pi h^3} - \frac{M}{h^9}, \quad (4.3)$$

where typical values $A = 1.7 \times 10^{-20}$ J and $M = 0.018 \varepsilon \sigma^6$ are used. This form of disjoining

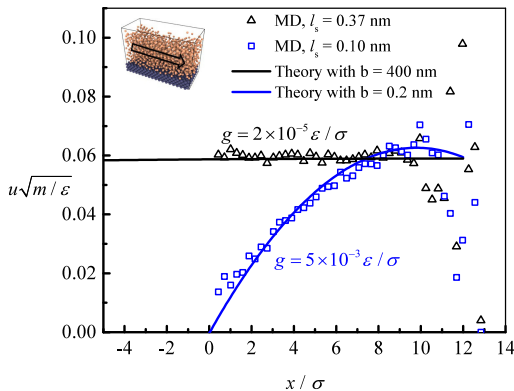


Figure 3: Slip length measured using pressure-driven flows past the substrate in molecular simulations. MD results of velocity (symbols) are fitted with analytical solutions (solid lines) to obtain slip length.

pressure $h^{-3} - h^{-9}$ is obtained by integrating the 12-6 LJ potential over the entire substrate assuming the substrate is continuous, as shown in Appendix and (Israelachvili 2011; Carey & Wemhoff 2005; Schick 1990; Dietrich *et al.* 1988; MacDowell *et al.* 2014). There are many other forms of disjoining potential resulting from different liquid and solid properties (Becker *et al.* 2003).

We vary the lattice spacing ℓ_s and see what the slip length is from independent simulations where a pressure-driven flow goes past a substrate as shown by the MD snapshot in figure 3. The pressure gradient is created by applying a body force g to the fluid. For $\ell_s = 0.37$ nm, one can see that the velocity profile in MD (blue squares in figure 3) is parabolic. However, for $\ell_s = 0.10$ nm, the velocity profile in MD (black triangles in figure 3) is nearly constant (plug flow).

The generated velocity distribution is

$$u(z) = \frac{\rho g}{2\mu} [(z - z_1)(2z_2 - z_1 - z) + 2b(z_2 - z_1)]. \quad (4.4)$$

Here $z_1 = 0$ and $z_2 = 9.2\sigma$ are the positions of the wall and the free surface respectively. This prediction (solid lines in figure 3) is used to fit the MD results (symbols in figure 3) to obtain the slip length. For $\ell_s = 0.37$ nm, a nearly no-slip surface $b = 0.2$ nm is achieved. For $\ell_s = 0.10$ nm, a strong slip length of $b = 400$ nm is obtained. Note that the choice of thermostats may influence the slip length a little. For example, for water flows inside carbon nanotubes, the Berendsen and Nosé-Hoover thermostats result in very similar slip length, while a smaller slip length is found under the influence of the Langevin thermostat (Sam *et al.* 2017). Thus, the same thermostats should be chosen when measuring the slip length from pressure-driven flows and simulating nanofilm dewetting.

To mimic experimental conditions of polymer films on OTS (octadecyltrichlorosilane) and DTS substrates (Lessel *et al.* 2017), where contact angles (disjoining pressure) are about the same for both cases but slip length is very different (no slip on OTS in contrast to 500 nm slip length on DTS), we thus keep the disjoining pressure (4.3) the same for the simulations of weak-slip nanofilm dewetting and strong-slip nanofilm dewetting. In our simulations, the contact angles of drops after film dewetting for both cases are measured to be about 40 degrees. This can also facilitate the comparison between weak-slip dewetting and strong-slip dewetting in simulations as the slip length is the only variable. Classically, disjoining pressure decreases with increasing slip length and contact angles. This is, however, far from being universal, as discussed above for the case of polymer films on OTS and DTS substrates.

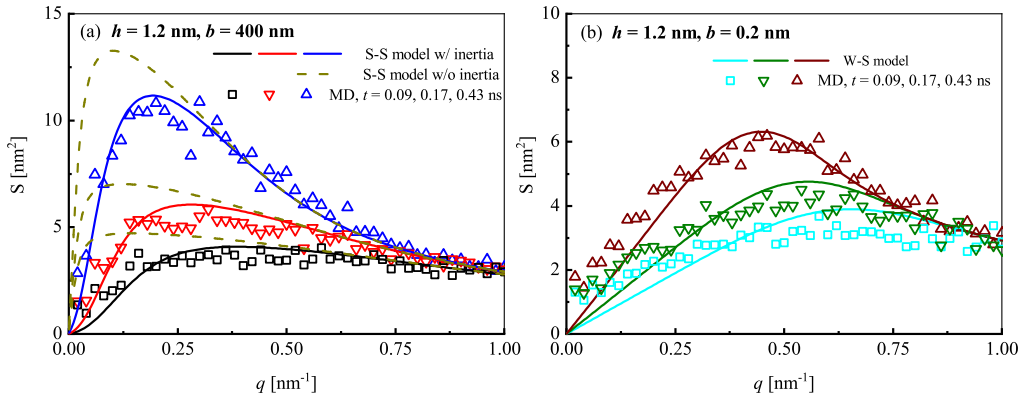


Figure 4: Evolution of the capillary spectra for the film with the thickness $h = 1.2$ nm at three different times. (a) the film has a strong slip length $b = 400$ nm. Solid lines represent the prediction of the full S-S model while dash lines are the S-S model without the inertial terms. (b) the film has a weak slip length $b = 0.2$ nm.

Liquids on hydrophilic substrates with small contact angles can also have large slip length (Ho *et al.* 2011; Rothstein 2010). As shown in Appendix, the proposed simulation technique is general and it can include the classic results where slip length and disjoining pressure are coupled and disjoining pressure decreases with increasing slip length and contact angles. As the virtual force is obtained by integrating the LJ potential (especially for f_x), this simulation technique is limited for the system where liquid and solid interact with LJ potential.

With the wall modelled by the virtual force, the simulations of nanofilm dewetting are run 2 ns for the case of $h_0 = 1.2$ nm, 10 ns for $h_0 = 1.6$ nm, and 100 ns for $h_0 = 3.14$ nm.

5. Results and Discussions

5.1. Evolving spectra of an unstable film with strong slip

As shown in figure 2, a flat film deposited on the substrate experiences the spontaneous growth of perturbations on its surface, leading to film rupture (see figure 2(b)) and droplet formation (see figure 2(c)). To reveal the instability mechanism in the case of the strong-slip dewetting, the evolution of its surface spectra is obtained from MD simulations.

The instantaneous liquid-vapour interface $h(x, t)$, defined by the usual equimolar surface, is extracted from MD simulations (see (Zhang *et al.* 2019) for methods). A discrete Fourier transform of $h(x, t)$ is performed to obtain the amplitude of surface modes $\hat{h}(q, t)$. The surface spectra are thus calculated from the average (root mean square) of 40 independent simulations.

The symbols in figure 4(a) represent the MD spectra for the film with thickness $h = 1.2$ nm and slip length $b = 400$ nm at three different times. Compared to the weak-slip case ($b = 0.2$ nm) presented in figure 4(b), one can see that the transient characteristics of the spectra are strongly influenced by the slip length. The spectra for the strong-slip case grow faster than the spectra for the weak-slip case by comparing the blue triangles in figure 4(a) with the wine triangles in figure 4(b). The dominant wavenumber q_d (the one with the maximum amplitude) at different times in the strong-slip dewetting are smaller than those in the weak-slip dewetting (e.g., at $t = 0.43$ ns, $q_d \approx 0.25$ nm⁻¹ for the strong-slip case in figure 4(a) in contrast to $q_d \approx 0.50$ nm⁻¹ for the weak-slip case in figure 4(b)).

The proposed stochastic models (S-S model and W-S model) and their analytical spectra are used to predict the MD spectra. In our MD simulations, the initial setting of the film

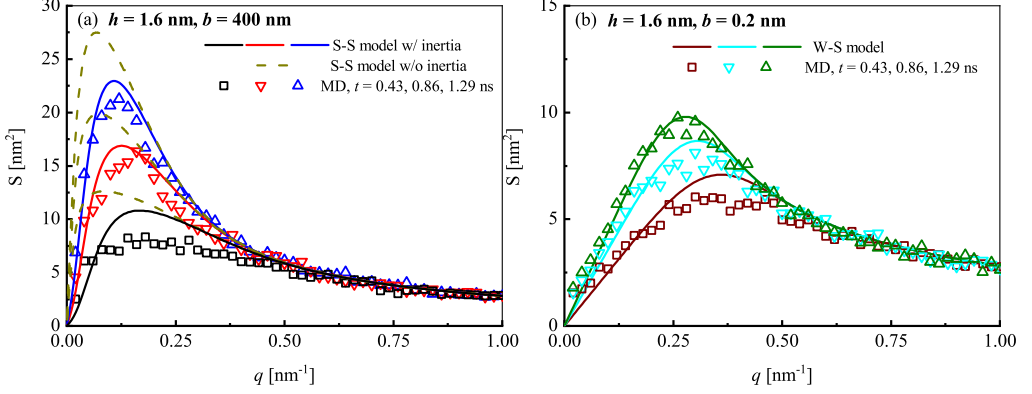


Figure 5: Evolution of the capillary spectra for the film with the thickness $h = 1.6$ nm at three different times. (a) the film has a strong slip length $b = 400$ nm. (b) the film has a weak slip length $h = 0.2$ nm.

surface is flat $|\hat{h}(q, 0)| \approx 0$, so that the deterministic contribution to the surface spectra is $|\hat{h}_{\text{det}}| \approx 0$. As elaborately investigated in our previous work (Zhang *et al.* 2019, 2021, 2020), the capillary spectra for weak-slip film can be predicted well by the W-S model, e.g., see the solid lines in figure 4(b). However, the W-S model does not apply to the case where the slip is strong, since the W-S model with $b = 400$ nm leads to enormous overpredictions compared to MD results (not shown). This is because the derivation of the W-S model requires the slip length on the order of the film thickness. To predict the spectra of the unstable film with strong slip $b = 400$ nm, the analytical spectra (3.13) of the newly derived S-S model is adopted and it agrees excellently with MD results (see the solid lines in figure 4(a)). The symbols in figure 5(a) show the MD spectra for the film with a larger thickness $h = 1.6$ nm. Again, our analytical spectra can predict the MD results very well. Note that for large wavenumbers, the spectra at different times simply collapse into the static spectrum $S_s = \sqrt{L_x k_B T / (L_y \gamma q^2)}$.

Another interesting finding is that the assumption of Stokes flow i.e., negligible inertia, breaks down when the value of slip length is increased from a weak slip to a strong slip. Ignoring the inertial terms in the derived S-S SLE (the left-hand-side terms of (2.27)), the surface spectra are simply

$$S(q, t) = \sqrt{\frac{L_x}{L_y} \frac{k_B T}{\gamma q^2 + d\phi/dh}} [1 - e^{-2Dt/C}], \quad (5.1)$$

which however overpredicts the MD results (see the dash line in figure 4(a) and 5(a)). Note that the W-S model where inertia is also absent works well for predicting the MD results of weak-slip dewetting. Therefore, it is the strong slip that brings the inertia into effect. In the weak-slip regime, the Reynolds number is

$$\text{Re}_{W-S} = \frac{\rho u_0 h_0}{\mu} = \chi^3 \frac{\rho \gamma h_0}{\mu^2} = \chi^3 La. \quad (5.2)$$

Here we have used the momentum balance in the horizontal direction to estimate the characteristic velocity $u_0 \sim \chi^3 \gamma / \mu$ as discussed before. However, in the strong-slip regime, the Re_{S-S} is

$$\text{Re}_{S-S} = \frac{\rho u_0 h_0}{\mu} = \chi \frac{\rho \gamma h_0}{\mu^2} = \chi La, \quad (5.3)$$

based on the momentum balance in the vertical direction. Therefore Re_{S-S} of the strong-slip

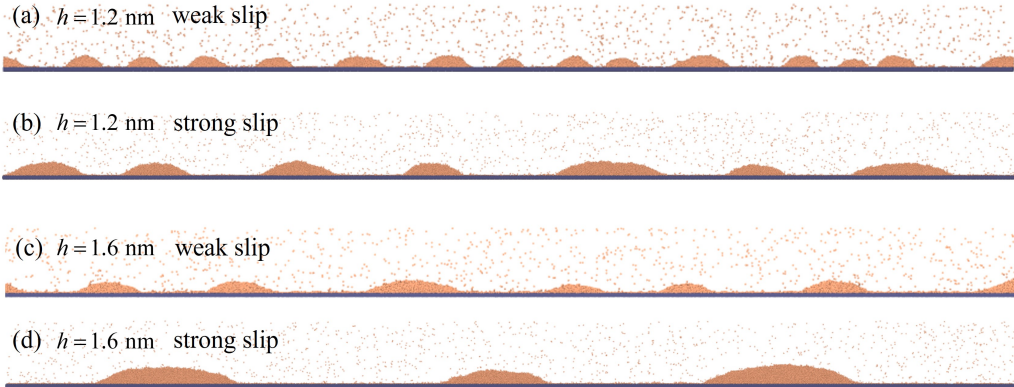


Figure 6: Droplets form after the rupture of the film. (a) for the film with $h = 1.2$ nm and $b = 0.2$ nm. (b) for the film with $h = 1.2$ nm and $b = 400$ nm. (c) for the film with $h = 1.6$ nm and $b = 0.2$ nm. (d) for the film with $h = 1.6$ nm and $b = 400$ nm.

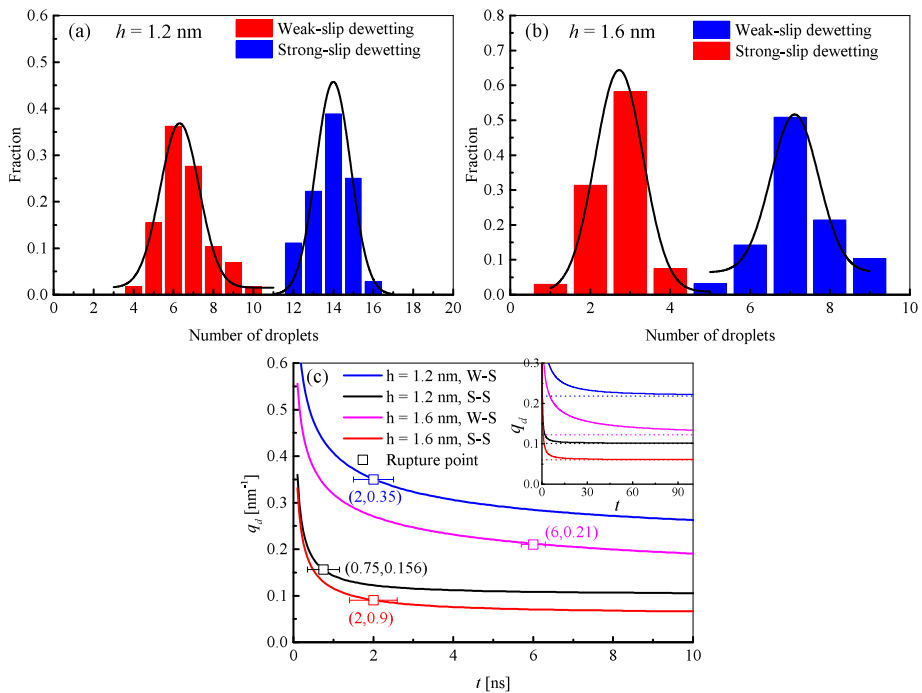


Figure 7: (a) Distribution of the number of droplets for the film with $h = 1.2$ nm. (b) Distribution of the number of droplets for the film with $h = 1.6$ nm. (c) The decrease of the dominant wavenumber with time predicted by the (3.13) (solid lines) to its asymptotic value by the deterministic lubrication equation (dash lines in the inset). The squares represent the dominant wavenumber at the time of film rupture.

case is $1/\chi^2$ larger than the weak-slip case. On the other hand, the Laplace number La in our simulations is calculated to be 0.3 which is consistent with the assumption of deriving the strong-slip model where the $La \sim 1$. Both conditions (strong slip and $La = 0.3$) make inertia non-negligible in our simulations.

5.2. Number of droplets

As shown in figure 6, one distinct feature of the strong-slip dewetting (see figures 6(b) and (d)) is having fewer droplets after the film ruptures compared to the weak-slip dewetting (see figures 6(a) and (c)). For each case with a specific film thickness and slip length (for example, in figure 6(a), $h = 1.2$ nm and $b = 0.2$ nm), about 40 independent simulations have been run and the probability distribution of the number of formed droplets is calculated and shown in figures 7(a) for $h = 1.2$ nm and 7(b) for $h = 1.6$ nm.

In terms of the thinner film $h = 1.2$ nm, the average number of droplets for weak-slip dewetting is $N_a = 14$ (see the blue bars in figure 7(a) and a typical MD snapshot in figure 6(a)), while the number is $N_b = 6.5$ for the strong-slip dewetting (see the red bars in figure 7(a) and a typical MD snapshot in figure 6(b)). For the thicker film with $h = 1.6$ nm, the mean number of droplets for weak-slip dewetting is $N_c = 7$ (see the blue bars in figure 7(b) and the MD snapshot in figure 6(c)) while the number is $N_d = 3$ for strong-slip dewetting (see the red bars in figure 7(b) and the MD snapshot in figure 6(d)).

The number of droplets is connected with the dominant wavenumber q_d (or the dominant wavelength $\lambda_d = 2\pi/q_d$). In the deterministic situation, the dominant wavenumber is constant over time. For the deterministic W-S equation, it is $q_d = \sqrt{-(d\phi/dh)/(2\gamma)} \approx \sqrt{A/(4\pi\gamma h_0^4)}$, while for the deterministic S-S equation, it is the solution when $d\omega_1(q)/dt = 0$.

However, as found from MD simulations shown in figure 4 and figure 5, the dominant wavenumber decreases with time, which is surely beyond the prediction from the deterministic lubrication equation. Based on the analytical spectra of the W-S model (3.14) and S-S model (3.13), figure 7(c) shows the theoretical prediction of the evolving dominant wavenumber. One can find that thermal fluctuations induce a dominant wavenumber (see the solid lines) much higher than its corresponding deterministic prediction (see the dash lines in the inset) and it only gradually decreases to the deterministic predictions over time. In our simulations, the film can rupture far before the dominant wavenumber reaches its asymptotic value.

Therefore, we measure the average time of rupture t_r from MD simulations (shown by the symbols in figure 7(c)) and use the analytical theory to predict the dominant wavenumber at the time of rupture. For $h = 1.2$ nm and $b = 0.2$ nm, the rupture time is about $t_r = 2$ ns and the dominant wavenumber at this time is $q_d = 0.35$ nm⁻¹. The dominant wavenumber corresponds to $q_d L_x / (2\pi) \approx 17$ droplets, in agreement with the 14 measured directly from MD simulations. For $h = 1.2$ nm and $b = 400$ nm, the rupture is much faster $t_r = 0.75$ ns and the dominant wavenumber at this time is $q_d = 0.156$ nm⁻¹. This dominant wavenumber translates into 7.8 droplets, in agreement with the 6.5 measured directly from MD simulations. Therefore increasing slip length from weak slip to strong slip can indeed reduce the number of droplets by decreasing the dominant wavenumber.

Since the strong-slip dewetting and the weak-slip dewetting starts with the same surface condition (flat surface), the deviations for both cases in the dominant wavenumber begin at a very early time (see figure 7(c)). The smaller dominant wavenumber in the strong-slip dewetting, compared with the weak-slip dewetting, becomes the obvious feature of the strong-slip spectra shown in figure 4(a).

By increasing the film thickness from $h = 1.2$ nm to $h = 1.6$ nm, the number of droplets is also decreased. For example, for the strong-slip dewetting, the average number of droplets changes from 6.5 to 3 by with increased film thickness as shown in figure 7(b). This can be also predicted by the dominant wavenumbers shown in figure 7(c) where the dominant wavenumber is smaller for a larger film thickness.

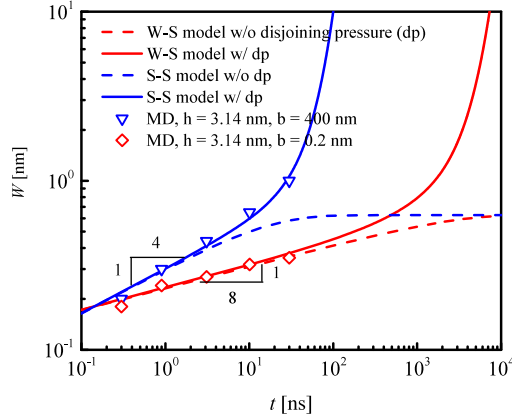


Figure 8: The growth of roughness on films with weak slip and strong slip.

5.3. Surface roughening with strong slip

The growth of spectra is equivalent to the surface roughening of the free surface based on Parseval's theorem:

$$W(t) = \sqrt{\frac{1}{L_x} \left\langle \int_0^{L_x} (\delta h)^2 dx \right\rangle} = \sqrt{\frac{1}{2\pi L_x} \int_{\frac{2\pi}{L_x}}^{\frac{2\pi K}{L_x}} S^2 dq}, \quad (5.4)$$

where $W(t) = \sqrt{\overline{h^2} - \bar{h}^2}$ is the root-mean-square roughness of the free surface. K is the number of bins used to extract the surface profile from MD simulations, which provides an upper bound on the wavenumbers that can be extracted (Zhang *et al.* 2021).

In our study, the roughening of a flat liquid surface is due to thermal fluctuations (and also disjoining pressure). Surface roughening or growth resulting from other forms of randomness is a common occurrence in nature. Examples include the propagation of wetting fronts in porous media, the growth of bacterial colonies, and the atomic deposition process in the manufacture of computer chips (Barabási & Stanley 1995). These evolutions of the profile of a growing interface can be described by stochastic partial differential equations (SPDE). One of the most famous examples is the Kardar–Parisi–Zhang (KPZ) equation (Kardar *et al.* 1986). Scaling relations for surface roughening are then used to analyze the SPDE, which can be summarized as (Barabási & Stanley 1995)

$$W(t) \sim L^\alpha f(t/L^m), \quad (5.5)$$

where L is the system size, $f(v) = v^\kappa$ for $v \ll 1$ (during roughness growth), and $f(v) = 1$ for $v \gg 1$ (at roughness saturation). The time to transition, between roughness growth and saturation, scales with $t_s \sim L^m$. The three exponents (α , m and κ) define a universality class, and are here related by $\kappa = \alpha/m$. For example, for the one-dimensional KPZ equation, ($\alpha = 1/2, m = 1/3, \kappa = 3/2$). Basically, the roughness will grow as a power law of time $W \sim t^\kappa$ before getting saturated, which is a result of the balance of the deterministic forces (such as surface tension in our study) and stochastic forces (such as thermal motions of molecules in our study).

In our previous work (Zhang *et al.* 2021), we have shown that for a weak-slip film roughened by thermal fluctuations (with negligible effects of disjoining pressure), a universality class ($\alpha = 1/2, m = 4, \kappa = 1/8$) exists and $W \sim t^{1/8}$ before the roughness saturation. It is interesting to see how strong slip changes the scaling of surface roughening. We note that

the existence of the disjoining pressure breaks the potential balance of surface tension and thermal fluctuations, resulting in the unbounded growth of the surface roughness. However, the initial growth of surface roughness, when the disjoining pressure is weak, may still be described by scaling laws.

As shown in figure 8, we calculate the surface roughening of a film with the thickness $h = 3.14$ nm for different levels of slip length. In terms of the weak-slip film $b = 0.2$ nm and without disjoining pressure, the roughness grows with $W \sim t^{1/8}$ and then becomes saturated eventually (see the blue dash line in figure 8). When disjoining pressure is considered, the growth of the roughness becomes unbounded (see the red solid line). However, the initial stage of the growth of roughness ($t < 100$ ns) is unaffected by disjoining pressure so that the $W \sim t^{1/8}$ is still valid.

For the strong-slip film $b = 400$ nm and without disjoining pressure, we find $W \sim t^{1/4}$ as shown by the blue dash line in figure 8, which can be derived as follows. α can be obtained by considering the surface at saturation, i.e. from the static spectrum given by $S_s = \sqrt{L_x k_B T / (L_y \gamma q^2)}$. Substituting the static spectrum into (5.4) leads to

$$W_s = \sqrt{\frac{1}{2\pi L_y} \frac{k_B T}{\gamma} \left(\frac{L_x}{2\pi} - \frac{L_x}{2\pi K} \right)}. \quad (5.6)$$

For large K , which is the case in our MD simulations, W_s becomes independent of K , and one can find that $W_s = \sqrt{\frac{L_x}{4\pi^2 L_y} \frac{k_B T}{\gamma}} \sim L_x^{1/2}$.

An upper estimate on the transition time $t_s \sim L^m$, between growth and saturation, can be estimated from the inverse of the dispersion relation at the largest permissible wavelength ($q = 2\pi/L_x$). Examining the dispersion relation indicates that there are three time scales for the spectra to reach thermal equilibrium (without disjoining pressure) whose maximum is the right time scale, namely,

$$\begin{aligned} t_s &= \frac{1}{\min(|2\omega_1(q = 2\pi/L_x)|, |2\omega_2(q = 2\pi/L_x)|, C(q = 2\pi/L_x))} \\ &= \frac{1}{|2\omega_1(q = 2\pi/L_x)|} \\ &\sim L_x^2, \end{aligned} \quad (5.7)$$

where we have used the condition $C = \frac{\mu}{\rho} \left(4q^2 + \frac{1}{h_0 b} \right) \approx \frac{4q^2 \mu}{\rho}$ due to the fact that $4q^2 h_0 b = 4/\chi \gg 1$ (using the long-wave condition $qh_0 \sim \chi$ and the strong-slip condition $bh_0 \sim \chi^{-2}$).

Therefore we find the power $m = 2$ and $\kappa = \alpha/m = 1/4$ for the strong-slip case. In summary, the university class ($\alpha = 1/2, m = 2, \kappa = 1/4$) is found for the surface growth of a thin film with strong slip and negligible disjoining pressure. When disjoining pressure is considered, the initial growth of the surface may still be described by $W \sim t^{1/4}$ (as shown by the blue solid line in figure 8), which is much faster than the $W \sim t^{1/8}$ of the weak-slip case. These scalings are confirmed in MD simulations (see the symbols in figure 8).

6. Conclusions

In this work, the instability of molecularly thin liquid films on substrates with strong slip is investigated using both molecular dynamics simulations and a newly developed stochastic lubrication equation. A new method is proposed to generate strong slip length in molecular simulations. Our simulations reveal that the strong-slip dewetting is much faster than the

weak-slip dewetting and has fewer droplets formed compared with the weak-slip dewetting. Using a long-wave approximation to the equations of fluctuating hydrodynamics, a new stochastic lubrication equation considering strong slip and inertia effects is derived. By the linear stability analysis, the analytical surface spectrum is obtained and it can explain the differences between strong-slip dewetting and weak-slip dewetting observed in simulations. We further find that inertial effects, which are usually ignored in weak-slip dewetting, come into play in the strong-slip dewetting due to the enhanced velocity by the strong slip.

When the effect of disjoining pressure is negligible, the derived strong-slip stochastic lubrication equation possesses a universality class $(1/2, 2, 1/4)$ in contrast to the $(1/2, 4, 1/8)$ of the weak-slip stochastic lubrication equation. In our simulations, the effect of disjoining pressure is important. However, the surface roughening of strong-slip dewetting at the initial stage may be still described by $W \sim t^{1/4}$ in contrast to the $W \sim t^{1/8}$ for weak-slip dewetting.

Experiments of the rupture of polymer nanofilms on *no-slip* SiO₂-coated silicon wafers have demonstrated the great effects of thermal fluctuations (Fetzer *et al.* 2007). The experimental surface spectra can be predicted with the *no-slip* film stochastic lubrication equation (Grün *et al.* 2006; Fetzer *et al.* 2007). However, polymer films on DTS solid can have slip length up to several micrometers (Bäumchen & Jacobs 2009). Therefore, experiments on the rupture of polymer nanofilms on DTS solid can be used to validate the newly developed theory here. However, care should be taken to make sure the dewetting of polymer films is initiated by disjoining pressure since polymer films can be easily contaminated (leading to nucleation dewetting) (Jacobs *et al.* 1998). As polymers have a very large viscosity $\sim 10^4$ kg/(ms), the Laplace number is very small so that the effects of inertia can be safely neglected. For metallic films, however, its viscosity is about $\sim 10^{-3}$ kg/(ms) so that inertial effects can be important (Diez *et al.* 2016; González *et al.* 2016).

In the limit of infinite slip, the derived strong-slip stochastic lubrication equation leads to a new model for free films, which can be readily used to study, for example, the symmetrical breakup of a foam film under the effects of thermal fluctuations (Erneux & Davis 1993; Vaynblat *et al.* 2001). In this work, we focus on the linear stability theory and molecular simulations of nanofilm dewetting, numerical solutions to these stochastic lubrication equations remain to be investigated in the future, e.g. see (Grün *et al.* 2006; Nescic *et al.* 2015; Diez *et al.* 2016; Durán-Olivencia *et al.* 2019; Shah *et al.* 2019; Zhao *et al.* 2020). Future directions may also include the effects of contamination (such as surfactants) (Zhang & Ding 2023) and evaporation (Oron *et al.* 1997; Craster & Matar 2009) on film stability which often occur at small scales.

Acknowledgement

We are grateful for the discussions with Detlef Lohse, Duncan Lockerby, James Sprittles, and Vincent Bertin. This work is supported by NWO under the project of ECCM KICKstart DE-NL 20002799.

Declaration of interests

The authors report no conflict of interest.

Appendix

In this Appendix, the process of obtaining f_x and f_z is explained based on the previous work in literature, e.g., Steele (1973); Barrat & Bocquet (1999); Hadjiconstantinou (2021). First, the molecular mechanism of disjoining pressure is reviewed briefly. For the 12-6

Leonard Jones potential between fluid atoms and solid atoms as shown by (4.1), the total interaction energy exerted on a liquid molecule by a semi-infinitely extended and continuous substrate with density n_s is (see p209 of Israelachvili (2011))

$$\begin{aligned}
 U_{tot}(D) &= \int_{z=D}^{z=\infty} \int_{x=0}^{x=\infty} \left(\frac{\alpha_u}{r^{12}} - \frac{\beta_u}{r^6} \right) 2\pi x n_s dx dz \\
 &= \int_{z=D}^{z=\infty} dz \int_{x=0}^{x=\infty} \left[\frac{\alpha_u}{(z^2 + x^2)^6} - \frac{\beta_u}{(z^2 + x^2)^3} \right] 2\pi x n_s dx dz \\
 &= \frac{\pi \alpha_u n_s}{45D^9} - \frac{\pi \beta_u n_s}{6D^3}.
 \end{aligned} \tag{A1}$$

Here D is the distance of the fluid atom to the solid surface. We use α_u and β_u for a more general case and one can have $\alpha_u = 4\epsilon\sigma^{12}$ and $\beta_u = 4\epsilon\sigma^6$ as (4.1). One can see that the gradient of this potential is a force that results in pressure variations inside the liquid such that $\nabla p = -n_l \nabla U_{tot}$ (Carey & Wemhoff 2005). Therefore, the pressure inside the liquid is

$$p(D) \equiv -n_l U_{tot} = \frac{\pi \beta_u n_s n_l}{6D^3} - \frac{\pi \alpha_u n_s n_l}{45D^9}. \tag{A2}$$

The disjoining pressure $\phi(h)$ on the film surface is then $p(D)$ evaluated at h :

$$\phi(h) \equiv p(h) \equiv -n_l U_{tot}(h) = \frac{\pi \beta n_s n_l}{6h^3} - \frac{\pi \alpha n_s n_l}{45h^9}, \tag{A3}$$

which is the $h^{-3} - h^{-9}$ kind of disjoining pressure used in this work with different prefactors there (see (4.3)) to account for contact angles close to the experimental values. Though (A3) is widely used, especially in the field of fluid dynamics, one has to keep in mind that it is an approximation (though being good) of the real disjoining pressure in the liquid. This is because its derivations ignore the structures of liquid-vapor interfaces or liquid-solid interfaces where the liquid density is not simply uniform (Schick 1990). In fact, the liquid-vapor interface may contribute additional disjoining pressure in the liquid, though it does not necessarily affect the film instability. We stress that there are two findings here. First, the cutoff distance are often used in molecular simulations to reduce computational costs. By doing this, the solid does not cause disjoining pressure at the liquid-vapor interface when the film thickness is larger than the cutoff distance as there are no interactions between the film surface and the solid substrate. Secondly, treating the solid as a *continuous* material with density n_s , which is the usual way to obtain disjoining pressure from intermolecular potentials as shown above, actually eliminates the drag force from the wall to the liquid in the direction parallel to the substrate, leading to *free slip*. Therefore, treating the solid as a discontinuous crystal to obtain the correct force, especially in the x direction, is necessary. This was done by Steele (1973). The total potential for a fluid particle (gas in Steele (1973)) above a multilayer solid crystal is

$$\begin{aligned}
 U_{tot} &= \frac{2\pi \epsilon_{gs}}{a_s} \sum_{\alpha} \left\{ q \left(\frac{2\sigma_{gs}^{12}}{5z_{\alpha}^{10}} - \frac{\sigma_{gs}^6}{z_{\alpha}^4} \right) + \dots \right. \\
 &\quad \left. + \sum_{g \neq 0} \sum_{k=1}^q \exp(i\vec{g} \cdot [\vec{m}_k + \vec{\tau}]) \times \left[\frac{\sigma_{gs}^{12}}{30} \left(\frac{g}{2z_{\alpha}} \right)^5 K_5(gz_{\alpha}) - 2\sigma_{gs}^6 \left(\frac{g}{2z_{\alpha}} \right)^2 K_2(gz_{\alpha}) \right] \right\}. \tag{A4}
 \end{aligned}$$

Here $a_s = \ell_s^2$ is the area of the unit lattice cell with a lattice spacing ℓ_s . α is the layer number of crystal layers and z_{α} is its location. $\vec{\tau}$ is the two-dimensional translation vector and \vec{g} is a multiple of the reciprocal lattice vectors. \vec{m} is a vector that gives the location of the k_{th} atom

in the unit cell. Basically, U_{tot} in (A4) can be split into two parts $U_0(z)$ and $U_1(xyz)$ (also see Barrat & Bocquet (1999)):

$$U_{tot}(xyz) = U_0(z) + U_1(xyz),$$

$$U_0(z) = \frac{2\pi}{a_s} \sum_{\alpha} \left\{ q \left(\frac{2}{5} \frac{\sigma_{gs}^{12}}{z_{\alpha}^{10}} - \frac{\sigma_{gs}^6}{z_{\alpha}^4} \right) \right\},$$

$$U_1(xyz) = \frac{2\pi\chi_{gs}}{a_s} \sum_{g \neq 0} \sum_{k=1}^q \exp(i\vec{g} \cdot [\vec{m}_k + \vec{\tau}]) \left[\frac{\sigma_{gs}^{12}}{30} \left(\frac{g}{2z_{\alpha}} \right)^5 K_5(gz_{\alpha}) - 2\sigma_{gs}^6 \left(\frac{g}{2z_{\alpha}} \right)^2 K_2(gz_{\alpha}) \right] \quad (\text{A5})$$

$$U_0(z) \text{ in the limit of a continuous solid with number density } n_s \text{ is } U_0 = \frac{2\pi n_s \varepsilon_{gs}}{3} \left[\frac{2}{15} \frac{\sigma_{gs}^{12}}{z^9} - \frac{\sigma_{gs}^6}{z^3} \right],$$

which is the same as (A1). In terms of $U_1(xyz)$, considering that only the potential from the first lattice layer and the shortest reciprocal lattice vectors is the most important (Barrat & Bocquet 1999; Hadjiconstantinou 2021), it can be simplified to

$$U_1(xyz) = \frac{2\pi\varepsilon_{gs}}{a_s} \left[\frac{\sigma_{gs}^{12}}{30} \left(\frac{\pi}{\ell_s z} \right)^5 K_5 \left(\frac{2\pi}{\ell_s} z \right) - 2\sigma_{gs}^6 \left(\frac{\pi}{\ell_s z} \right)^2 K_2 \left(\frac{2\pi}{\ell_s} z \right) \right] \left[\cos \left(\frac{2\pi}{\ell_s} x \right) + \cos \left(\frac{2\pi}{\ell_s} y \right) \right] \quad (\text{A6})$$

Finally, the potential exerted by the wall to each fluid atom that we used in the work is (the y direction may be ignored if the simulation is (quasi) two dimensional)

$$U_{tot}(xz) = \frac{2\pi\varepsilon_{gs}}{3} \left[\frac{2}{15} \frac{\sigma_{gs}^{12}}{z^9} C_1 - \frac{\sigma_{gs}^6}{z^3} C_2 \right] + \dots \\ + C_3 \frac{2\pi\varepsilon_{gs}}{a_s} \left[\frac{\sigma_{gs}^{12}}{30} \left(\frac{\pi}{\ell_s z} \right)^5 K_5 \left(\frac{2\pi}{\ell_s} z \right) - 2\sigma_{gs}^6 \left(\frac{\pi}{\ell_s z} \right)^2 K_2 \left(\frac{2\pi}{\ell_s} z \right) \right] \cos \left(\frac{2\pi}{\ell_s} x \right), \quad (\text{A7})$$

where we have added factors C_1, C_2 , and C_3 so that they can be tuned ($C_3 = 1/100$ in this work) for the slip length, disjoining pressure, and contact angles reported in literature. More generally, we can use the function of disjoining pressure to replace the first term in (A7), namely, the total potential $U_0 = -\frac{\phi(z)}{n_l}$. The force expressed in (4.2) is thus $f_x = -dU_1(xz)/dx$ (also see Barrat & Bocquet (1999) and $f_z = -dU_0/dz$. If one wants that the slip length and disjoining pressure to be coupled, one can use (A7) with $C_1 = C_2 = C_3 = 1$ where slip length increases with contact angles but disjoining pressure decreases with increasing slip length.).

REFERENCES

- AARTS, DIRK GAL, SCHMIDT, MATTHIAS & LEKKERKERKER, HENK NW 2004 Direct visual observation of thermal capillary waves. *Science* **304** (5672), 847–850.
- BARABÁSI, A-L & STANLEY, HARRY EUGENE 1995 *Fractal Concepts in Surface Growth*. Cambridge University Press.
- BARRAT, JEAN-LOUIS & BOCQUET, LYDÉRIC 1999 Influence of wetting properties on hydrodynamic boundary conditions at a fluid/solid interface. *Faraday Discuss.* **112**, 119–128.
- BÄUMCHEN, OLIVER, FETZER, RENATE & JACOBS, KARIN 2009 Reduced interfacial entanglement density affects the boundary conditions of polymer flow. *Phys. Rev. Lett.* **103** (24), 247801.
- BÄUMCHEN, OLIVER & JACOBS, KARIN 2009 Slip effects in polymer thin films. *J. Phys. Condens.* **22** (3), 033102.
- BÄUMCHEN, OLIVER, MARQUANT, LUDOVIC, BLOSSEY, RALF, MÜNCH, ANDREAS, WAGNER, BARBARA &

- JACOBS, KARIN 2014 Influence of slip on the rayleigh-plateau rim instability in dewetting viscous films. *Phys. Rev. Lett.* **113** (1), 014501.
- BECKER, JÜRGEN, GRÜN, GÜNTHER, SEEMANN, RALF, MANTZ, HUBERT, JACOBS, KARIN, MECKE, KLAUS R & BLOSSEY, RALF 2003 Complex dewetting scenarios captured by thin-film models. *Nat. Mater.* **2** (1), 59.
- BOCQUET, LYDÉRIC & BARRAT, JEAN-LOUIS 1994 Hydrodynamic boundary conditions, correlation functions, and kubo relations for confined fluids. *Phys. Rev. E* **49** (4), 3079.
- BOCQUET, LYDÉRIC & CHARLAIX, ELISABETH 2010 Nanofluidics, from bulk to interfaces. *Chem. Soc. Rev.* **39** (3), 1073–1095.
- BUFF, FP, LOVETT, RA & STILLINGER JR, FH 1965 Interfacial density profile for fluids in the critical region. *Phys. Rev. Lett.* **15** (15), 621.
- CAREY, VP & WEMHOFF, AP 2005 Disjoining pressure effects in ultra-thin liquid films in micropassages: Comparison of thermodynamic theory with predictions of molecular dynamics simulations. In *ASME Int. Mech. Eng. Congress Expo.*, , vol. 42223, pp. 511–520.
- CARLSON, ANDREAS 2018 Fluctuation assisted spreading of a fluid filled elastic blister. *J. Fluid Mech.* **846**, 1076–1087.
- CRASTER, RICHARD V & MATAR, OMAR K 2009 Dynamics and stability of thin liquid films. *Rev. Mod. Phys.* **81** (3), 1131.
- DAVIDOVITCH, BENNY, MORO, ESTEBAN & STONE, HOWARD A 2005 Spreading of viscous fluid drops on a solid substrate assisted by thermal fluctuations. *Phys. Rev. Lett.* **95** (24), 244505.
- DIETRICH, S, DOMB, C & LEBOWITZ, JL 1988 Phase transitions and critical phenomena.
- DIEZ, JAVIER A, GONZÁLEZ, ALEJANDRO G & FERNÁNDEZ, ROBERTO 2016 Metallic-thin-film instability with spatially correlated thermal noise. *Phys. Rev. E* **93** (1), 013120.
- DING, ZIJING & WONG, TECK NENG 2015 Falling liquid films on a slippery substrate with marangoni effects. *Int. J. Heat Mass Transf.* **90**, 689–701.
- DURÁN-OLIVENCIA, MIGUEL A, GVALANI, RISHABH S, KALLIADASIS, SERAFIM & PAVLIOTIS, GRIGORIOS A 2019 Instability, rupture and fluctuations in thin liquid films: Theory and computations. *J. Stat. Phys.* **174** (3), 579–604.
- EGGERS, JENS 2002 Dynamics of liquid nanojets. *Phys. Rev. Lett.* **89** (8), 084502.
- EGGERS, JENS & DUPONT, TODD F 1994 Drop formation in a one-dimensional approximation of the navier-stokes equation. *J. Fluid Mech.* **262**, 205–221.
- ERNEUX, THOMAS & DAVIS, STEPHEN H 1993 Nonlinear rupture of free films. *Phys. Fluids* **5** (5), 1117–1122.
- FALK, KERSTIN, SEDLMEIER, FELIX, JOLY, LAURENT, NETZ, ROLAND R & BOCQUET, LYDÉRIC 2010 Molecular origin of fast water transport in carbon nanotube membranes: superlubricity versus curvature dependent friction. *Nano Lett.* **10** (10), 4067–4073.
- FETZER, RENATE, JACOBS, K, MÜNCH, A, WAGNER, B & WITELSKI, TP 2005 New slip regimes and the shape of dewetting thin liquid films. *Phys. Rev. Lett.* **95** (12), 127801.
- FETZER, RENATE, RAUSCHER, M, SEEMANN, R, JACOBS, KARIN & MECKE, KLAUS 2007 Thermal noise influences fluid flow in thin films during spinodal dewetting. *Phys. Rev. Lett.* **99** (11), 114503.
- GONZÁLEZ, ALEJANDRO G, DIEZ, JAVIER A & SELLIER, MATHIEU 2016 Inertial and dimensional effects on the instability of a thin film. *J. Fluid Mech.* **787**, 449–473.
- GRÜN, GÜNTHER, MECKE, KLAUS & RAUSCHER, MARKUS 2006 Thin-film flow influenced by thermal noise. *J. Stat. Phys.* **122** (6), 1261–1291.
- HADJICONSTANTINOY, NG 2021 An atomistic model for the navier slip condition. *J. Fluid Mech.* **912**, A26.
- HENNEQUIN, Y, AARTS, DGAL, VAN DER WIEL, JH, WEGDAM, G, EGGERS, J, LEKKERKERKER, HNW & BONN, DANIEL 2006 Drop formation by thermal fluctuations at an ultralow surface tension. *Phys. Rev. Lett.* **97** (24), 244502.
- HO, TUAN ANH, PAPAVALASSIOU, DIMITRIOS V, LEE, LLOYD L & STRIOLO, ALBERTO 2011 Liquid water can slip on a hydrophilic surface. *Proc. Natl. Acad. Sci.* **108** (39), 16170–16175.
- HÖFLING, FELIX & DIETRICH, SIEGFRIED 2015 Enhanced wavelength-dependent surface tension of liquid-vapour interfaces. *Europhys. Lett.* **109** (4), 46002.
- HÖFLING, FELIX & DIETRICH, SIEGFRIED 2020 Finite-size corrections for the static structure factor of a liquid slab with open boundaries. *J. Chem. Phys.* **153** (5).
- HÖFLING, FELIX & DIETRICH, SIEGFRIED 2024 Structure of liquid–vapor interfaces: Perspectives from liquid state theory, large-scale simulations, and potential grazing-incidence x-ray diffraction. *J. Chem. Phys.* **160** (10).
- ISRAELACHVILI, J. N. 2011 *Intermolecular and Surface Forces, 3rd ed.*. Academic Press.

- JACOBS, KARIN, HERMINGHAUS, STEPHAN & MECKE, KLAUS R 1998 Thin liquid polymer films rupture via defects. *Langmuir* **14** (4), 965–969.
- JHON, MYUNG S, PHILLIPS, DAVID M, VINAY, STEPHEN J & MESSER, CHRISTOPHER T 1999 The dynamic behavior of thin-film lubricants. *IEEE Trans. Magn.* **35** (5), 2334–2337.
- KARDAR, MEHRAN, PARISI, GIORGIO & ZHANG, YI-CHENG 1986 Dynamic scaling of growing interfaces. *Phys. Rev. Lett.* **56** (9), 889.
- KARGUPTA, KAJARI, SHARMA, ASHUTOSH & KHANNA, RAJESH 2004 Instability, dynamics, and morphology of thin slipping films. *Langmuir* **20** (1), 244–253.
- LANDAU, LD & LIFSHITZ, EM 1959 *Course of Theoretical Physics. vol. 6: Fluid mechanics*. London.
- LAUGA, ERIC, BRENNER, MICHAEL P & STONE, HOWARD A 2005 Microfluidics: the no-slip boundary condition. *arXiv preprint cond-mat/0501557*.
- LESSEL, MATTHIAS, MCGRAW, JOSHUA D, BÄUMCHEN, OLIVER & JACOBS, KARIN 2017 Nucleated dewetting in supported ultra-thin liquid films with hydrodynamic slip. *Soft Matter* **13** (27), 4756–4760.
- LIAO, YING-CHIH, LI, YEN-CHING & WEI, HSIEN-HUNG 2013 Drastic changes in interfacial hydrodynamics due to wall slippage: slip-intensified film thinning, drop spreading, and capillary instability. *Phys. Rev. Lett.* **111** (13), 136001.
- LOHSE, DETLEF & ZHANG, XUEHUA 2015 Surface nanobubbles and nanodroplets. *Rev. Mod. Phys.* **87** (3), 981.
- MACDOWELL, LUIS G 2017 Capillary wave theory of adsorbed liquid films and the structure of the liquid-vapor interface. *Phys. Rev. E* **96** (2), 022801.
- MACDOWELL, LUIS G, BENET, JORGE, KATCHO, NEBIL A & PALANCO, JOSE MG 2014 Disjoining pressure and the film-height-dependent surface tension of thin liquid films: New insight from capillary wave fluctuations. *Adv. Colloid Interface Sci.* **206**, 150–171.
- MARBACH, SOPHIE, DEAN, DAVID S & BOCQUET, LYDÉRIC 2018 Transport and dispersion across wiggling nanopores. *Nat. Phys.* **14** (11), 1108–1113.
- MARTÍNEZ-CALVO, ALEJANDRO, MORENO-BOZA, DANIEL & SEVILLA, A 2020 The effect of wall slip on the dewetting of ultrathin films on solid substrates: Linear instability and second-order lubrication theory. *Phys. Fluids* **32** (10), 102107.
- MECKE, KLAUS & RAUSCHER, MARKUS 2005 On thermal fluctuations in thin film flow. *J. Stat. Phys.* **17** (45), S3515.
- MOSELER, MICHAEL & LANDMAN, UZI 2000 Formation, stability, and breakup of nanojets. *Science* **289** (5482), 1165–1169.
- MÜNCH, ANDREAS, WAGNER, BA & WITELSKI, THOMAS P 2005 Lubrication models with small to large slip lengths. *J. Eng. Math.* **53**, 359–383.
- NESIC, S, CUERNO, R, MORO, E & KONDIC, L 2015 Fully nonlinear dynamics of stochastic thin-film dewetting. *Phys. Rev. E* **92** (6), 061002(R).
- ORON, ALEXANDER, DAVIS, STEPHEN H & BANKOFF, S GEORGE 1997 Long-scale evolution of thin liquid films. *Rev. Mod. Phys.* **69** (3), 931.
- PLIMPTON, STEVE 1995 Fast parallel algorithms for short-range molecular dynamics. *J. Comput. Phys.* **117** (1), 1–19.
- ROTHSTEIN, JONATHAN P 2010 Slip on superhydrophobic surfaces. *Annu. Rev. Fluid Mech.* **42**, 89–109.
- SAM, ALAN, KANNAM, SRIDHAR KUMAR, HARTKAMP, REMCO & SATHIAN, SARITH P 2017 Water flow in carbon nanotubes: The effect of tube flexibility and thermostat. *J. Chem. Phys.* **146** (23).
- SAVVA, NIKOS, KALLIADASIS, SERAFIM & PAVLIOTIS, GRIGORIOS A 2010 Two-dimensional droplet spreading over random topographical substrates. *Phys. Rev. Lett.* **104** (8), 084501.
- SCHICK, M 1990 Liquids at interfaces. *Les houches session XLVIII* pp. 419–96.
- SEEMANN, RALF, HERMINGHAUS, STEPHAN & JACOBS, KARIN 2001 Dewetting patterns and molecular forces: A reconciliation. *Phys. Rev. Lett.* **86** (24), 5534.
- SHAH, MAULIK S, VAN STEIJN, VOLKERT, KLEIJN, CHRIS R & KREUTZER, MICHIEL T 2019 Thermal fluctuations in capillary thinning of thin liquid films. *J. Fluid Mech.* **876**, 1090–1107.
- SIBLEY, DAVID N, NOLD, ANDREAS, SAVVA, NIKOS & KALLIADASIS, SERAFIM 2015 A comparison of slip, disjoining pressure, and interface formation models for contact line motion through asymptotic analysis of thin two-dimensional droplet spreading. *J. Eng. Math.* **94**, 19–41.
- STEELE, WILLIAM A 1973 The physical interaction of gases with crystalline solids: I. gas-solid energies and properties of isolated adsorbed atoms. *Surf. Sci.* **36** (1), 317–352.
- STONE, HOWARD A, STROOCK, ABRAHAM D & AJDARI, ARMAND 2004 Engineering flows in small devices: microfluidics toward a lab-on-a-chip. *Annu. Rev. Fluid Mech.* **36**, 381–411.

- THOMPSON, PETER A & ROBBINS, MARK O 1990 Origin of stick-slip motion in boundary lubrication. *Science* **250** (4982), 792–794.
- VAYNBLAT, DIMITRI, LISTER, JOHN R & WITELSKI, THOMAS P 2001 Rupture of thin viscous films by van der Waals forces: Evolution and self-similarity. *Phys. Fluids* **13** (5), 1130–1140.
- VRIJ, A & OVERBEEK, J TH G 1968 Rupture of thin liquid films due to spontaneous fluctuations in thickness. *J. Am. Chem. Soc.* **90** (12), 3074–3078.
- WEINSTEIN, STEVEN J & RUSCHAK, KENNETH J 2004 Coating flows. *Annu. Rev. Fluid Mech.* **36**, 29–53.
- WILLIS, ADAM M & FREUND, JB 2009 Enhanced droplet spreading due to thermal fluctuations. *J. Condens. Matter Phys.* **21** (46), 464128.
- XIE, R, KARIM, ALAMGIR, DOUGLAS, JACK F, HAN, CHARLES C & WEISS, ROBERT A 1998 Spinodal dewetting of thin polymer films. *Phys. Rev. Lett.* **81** (6), 1251.
- ZHANG, YIXIN & DING, ZIJING 2023 Capillary nanowaves on surfactant-laden liquid films with surface viscosity and elasticity. *Phys. Rev. Fluids* **8** (6), 064001.
- ZHANG, YIXIN, SPRITTLES, JAMES E & LOCKERBY, DUNCAN A 2019 Molecular simulation of thin liquid films: Thermal fluctuations and instability. *Phys. Rev. E* **100** (2), 023108.
- ZHANG, YIXIN, SPRITTLES, JAMES E & LOCKERBY, DUNCAN A 2020 Nanoscale thin-film flows with thermal fluctuations and slip. *Phys. Rev. E* **102** (5), 053105.
- ZHANG, YIXIN, SPRITTLES, JAMES E & LOCKERBY, DUNCAN A 2021 Thermal capillary wave growth and surface roughening of nanoscale liquid films. *J. Fluid Mech.* **915**.
- ZHAO, CHENGXI, LOCKERBY, DUNCAN A & SPRITTLES, JAMES E 2020 Dynamics of liquid nanothreads: Fluctuation-driven instability and rupture. *Phys. Rev. Fluids* **5** (4), 044201.
- ZHAO, CHENGXI, SPRITTLES, JAMES E & LOCKERBY, DUNCAN A 2019 Revisiting the rayleigh–plateau instability for the nanoscale. *J. Fluid Mech.* **861**.